

**Structure and ordering of oxygen on unreconstructed Ir(100)**

P. Ferstl, T. Schmitt, M. A. Schneider, and L. Hammer\*

*Solid State Physics, Friedrich-Alexander-University, Erlangen-Nürnberg, D-91058 Erlangen, Germany*

A. Michl and S. Müller

*Institute of Advanced Ceramics, Hamburg University of Technology, D-21073 Hamburg, Germany*

(Received 23 December 2015; revised manuscript received 13 May 2016; published 3 June 2016)

The adsorption of oxygen on the unreconstructed Ir(100) surface is investigated by a combination of experimental and theoretical methods comprising low-energy electron diffraction (LEED), scanning tunneling microscopy (STM), and density-functional theory (DFT). Apart from the well-known  $(2 \times 1)$ -O phase, we find a new  $(3 \times 1)$ -O phase for temperatures below 180 K. Our DFT calculations predict these two phases to be the only fundamental ground states of the system in the coverage range up to 0.5 monolayers. An analysis of the phase transitions as a function of coverage reveals extended coexistence ranges between the clean surface and the  $3 \times 1$  phase, or between the  $3 \times 1$  and  $2 \times 1$  phases, respectively. As a function of temperature, both phases undergo order-disorder transitions at about 650 K for the  $2 \times 1$  phase and 180 K for the  $3 \times 1$  phase, the latter being only partially reversible. The complete ordering behavior can be consistently explained by the energetics of model defect structures calculated by DFT. The crystallographic structure of the phases is determined by full-dynamical LEED intensity analyses, yielding excellent agreement between experimental and calculated data sets (Pendry  $R$ -factors:  $R_p \approx 0.1$ ). Oxygen was found to assume bridge sites always inducing significant relaxations within the substrate. The derived structural parameters coincide with the respective predictions from DFT on the picometer scale. It is also shown that remnants and precursor stages of the clean surface's reconstruction can only be detected through the application of real-space methods such as STM. The overarching objective of the present study is to demonstrate how precisely and accurately such an adsorption system can be investigated nowadays by using a concerted experimental and theoretical approach.

DOI: [10.1103/PhysRevB.93.235406](https://doi.org/10.1103/PhysRevB.93.235406)**I. INTRODUCTION**

Iridium as well as other late  $5d$  and  $4d$  metals are interesting catalyst materials in particular for CO oxidation and hydrocarbon reforming reactions. Detailed knowledge of the adsorption behavior of adsorbates such as oxygen, hydrogen, or carbon monoxide is a prerequisite for any understanding of their catalytic reaction with coadsorbates on the atomic scale. From a structural point of view, the (100) surfaces of Ir, Pt, and Au are of special interest, because their top layer shows an extra-dense quasihexagonal reconstruction when clean [1–5], whereby the  $5 \times 1$  superstructure of Ir(100) exhibits by far the most simple surface unit cell. The driving mechanism for this reconstruction is the aim to increase the coordination number of surface atoms, and therefore it becomes unstable upon chemisorption of practically all reactive gases, such as, e.g.,  $O_2$ , CO,  $CO_2$ , and even  $H_2$  [6–9]. For lifting the reconstruction, however, extra Ir atoms (0.2 ML) have to be expelled from the surface layer. For not too high temperatures, where Ir diffusion is limited, they will remain on the surface terraces as adatoms or small islands and thus can affect the adsorption and ordering properties of the adsorbates. Since they are in general nonperiodic, they can only be detected and studied by real-space methods such as scanning tunneling microscopy (STM), which has not been done so far.

The adsorption of oxygen on both the reconstructed and unreconstructed Ir(100) surface was investigated by Grant [6], who reported on a  $2 \times 1$  superstructure. This phase has

since been corroborated and quantitatively investigated by several groups [7,10–12]. Occasionally, another ordered phase with  $10 \times 2$  periodicity has also been observed after partial desorption of oxygen [7,9]. This phase, however, is due to the incipient surface reconstruction, as we will show in a forthcoming paper [13], leaving the  $2 \times 1$  phase the only ordered phase on the *unreconstructed* Ir(100) surface found so far in experiment. The structure of this  $2 \times 1$  phase has been investigated via a low-energy electron diffraction (LEED) intensity analysis and accompanying density-functional theory (DFT) calculations [11], with the result that oxygen atoms are adsorbed on bridge sites of the Ir substrate lattice inducing a local widening in the first and a buckling in the second layer. In a more recent study [12], additional partial occupation of hollow sites between the oxygen rows was reported for higher coverages ( $\theta > 0.5$ ). Total energy calculations have also been performed for several hypothetical ordered phases in addition to the  $2 \times 1$  phase, and various properties of these phases were discussed [11,14,15]. However, their stability, i.e., the question of whether these phases are ground states of the system or not, has not been investigated as of yet.

In the present study, we combine a DFT ground-state search in the coverage regime up to 0.5 ML with an experimental scan of the phase regime as a function of coverage and temperature. For the latter, we do not rely merely on diffraction methods (here LEED), but we also provide real-space information from STM measurements, in particular to investigate the homogeneity of the surface after the oxygen-induced lifting of the reconstruction. Our theoretical and experimental results are in perfect agreement and show that there are exactly two ordered phases: the known  $2 \times 1$  phase and a newly found  $3 \times 1$

\*lutz.hammer@fau.de

phase. After a description of the experimental and theoretical procedures (Sec. II), we first discuss the energetics of the whole accessible adsorption system as derived from the DFT calculations (Sec. III) before we describe the experimental appearance and stability of the ordered phases with respect to coverage and temperature (Sec. IV). Here we start with the easy-to-prepare  $2 \times 1$  phase at saturation coverage (Sec. IV A) and then turn toward lower oxygen coverages (Sec. IV B). Finally, we present the detailed crystallographic structure of the two phases determined by LEED intensity analyses (Sec. V) that turn out to be in perfect agreement with theory, and we close with a conclusion.

## II. EXPERIMENTAL AND COMPUTATIONAL DETAILS

### A. Laboratory equipment

The great majority of experiments were performed in an ultrahigh-vacuum chamber consisting of two separately pumped segments. One of them hosts a beetle-type scanning tunneling microscope operated at room temperature at very low ambient pressure ( $\approx 2 \times 10^{-11}$  mbar). The bias voltage was applied to the sample and typically set to values of 40–400 meV (current:  $I \approx 1$  nA). The other part of the chamber, typically operated at a pressure in the low  $10^{-10}$  mbar range, is equipped with a home-made LEED optics, a quadrupole mass spectrometer with a Feulner cup [16] for thermodesorption measurements, and equipment for sample preparation such as a plasma source for ion sputtering of the sample and various leak valves for a gas inlet. The latter allowed for either backfilling the chamber by high-purity gases for continuous LEED observation during dosage, or large gas exposures by means of a nozzle close to the Ir crystal's surface. This provided a vastly reduced gas load of the chamber (more than two orders of magnitude in local pressure between sample and chamber). Since part of the chamber's walls were used as a Ti sublimation pump, every gas exposure leads to an inhomogeneous pressure distribution within the chamber, and hence absolute values for the exposure cannot be reliably determined.

The sample was mounted on a holder that could easily be transferred between both chambers. In the LEED chamber, the sample stage allowed for rapid heating to temperatures up to 1500 K via electron bombardment from the rear and cooling with liquid nitrogen to about 90 K within minutes. The temperature was measured by a chromel-alumel thermocouple directly attached to the Ir crystal, and a thermocontroller driving the power supply of the heater allowed for linear temperature ramps in the range 0.1–10 K/s for TDS measurements. STM images were also taken at 77 K using a different apparatus, which was similarly equipped as described above, but with a home-built low-temperature STM.

### B. Sample preparation

The sample was initially cleaned by repeated cycles of ion sputtering ( $\text{Ne}^+$ , 2 keV,  $\approx 10 \mu\text{A}/\text{cm}^2$ ) and subsequent annealing in  $\text{O}_2$  at 1300 K until homogeneously reconstructed and widely defect-free terraces of almost  $\mu\text{m}$ -size developed in STM (cf. Ref. [5]) leading to a clear and low-background LEED pattern of the Ir(100)  $5 \times 1$  reconstruction as well.

During the experimental run, simple flashing to beyond 1300 K, with once-a-day short-time  $\text{O}_2$  annealing, was usually sufficient to restore the high-quality preparation of the surface reconstruction.

The unreconstructed  $1 \times 1$  phase as the starting point for most oxygen adsorption experiments was prepared following standard recipes [5,7,11,17]: The sample was first heated to 1300 K in front of the gas nozzle at a local  $\text{O}_2$  pressure in the  $10^{-6}$  mbar range and then cooled down to room temperature ( $\approx 10$  K/s) under continuous  $\text{O}_2$  flux. After recovery of the low ambient pressure in the chamber, the crystal was finally heated to 550 K and the oxygen effectively reduced by dosing  $\text{H}_2$  onto the surface ( $\leq 1$  L turned out to be sufficient). This procedure results in a clear  $1 \times 1$  LEED pattern, and large-scale STM images reveal a homogeneously unreconstructed clean surface with only a small number of vacancy islands (density  $\approx 0.01 \text{ nm}^{-2}$ ).

### C. LEED structure analyses

LEED intensity measurements were always performed at normal incidence of the primary electron beam (accuracy of the alignment  $\approx 0.2^\circ$ ) with the sample cooled to about 100 K in order to reduce thermal diffuse background intensity. LEED patterns were recorded by a CCD camera every 0.5 eV in the energy range 50–700 eV and stored on a computer. The whole data acquisition lasted about 10 min so that residual gas contaminations were negligible. In an offline evaluation, background-corrected integral spot intensities as a function of energy [ $I(E)$  spectra] were collected from this stack of frames for all accessible diffraction beams using an automated acquisition system [18]. Subsequently, the  $I(E)$  spectra of symmetrically equivalent beams were averaged, moderately smoothed where necessary to remove residual noise, normalized by the primary beam current, which was measured in parallel, and finally corrected for the cosine of the respective viewing angle.

The calculation of intensity spectra for model structures was performed using the TENSERLEED program package [19]. The large energy range up to 700 eV required the usage of phase shifts up to  $l_{\text{max}} = 14$  calculated by the program package EEASISS [20] for surface slabs with atomic positions close to the final fit geometries. This program also provides a self-consistently calculated energy-dependent inner potential  $V_{0r}$ . Electron attenuation was simulated by a constant optical potential  $V_{0i}$ , which was fitted in the  $2 \times 1$  analysis as  $V_{0i} = 5.75$  eV and adopted for the  $3 \times 1$  analysis as well. The lateral lattice parameter of iridium was set to  $a_p = 2.7116 \text{ \AA}$  [21] and the Ir bulk vibrational amplitude was calculated [22] from the Debye temperature of 430 K. For a quantitative comparison of experimental and calculated intensity spectra, the Pendry  $R$ -factor [23]  $R_P$  was applied and its variance  $\text{var}(R_P)$  was used to estimate the statistical errors of the fit parameters by one-parameter variation.

In the course of the LEED analyses, structural parameters down to the sixth Ir layer were varied in order to properly describe the strain field induced within the Ir substrate. Also vibrational amplitudes for oxygen and first-layer Ir atoms were fitted as well as a constant shift of the energy scale to account for the cathode's work function. The fitting procedures were

always completed by a final “fine-tuning” step for which a new structural search was performed in a very narrow range around the former best-fit configuration with a grid width as small as 0.0025 Å for atomic positions and vibrational amplitudes. Additionally, the final parameter configuration of the TENSORLEED search procedure was always verified by a subsequent fully dynamical LEED calculation.

#### D. DFT calculations

The DFT calculations were performed with the VASP [24–27] code using the projector augmented wave (PAW) method [28,29]. A plane-wave cutoff of 550 eV was chosen, and exchange correlation effects were treated within the PBE [30] approximation. We employed second-order Methfessel-Paxton [31] smearing with a smearing width of 0.15 eV. With these parameters, we obtain a lattice parameter of 3.877 Å for bulk Ir, which is only 1% larger than the experimental value [21]. Oxygen adsorption was modeled by symmetric surface slabs with 11 Ir layers separated by the equivalent of 10 vacuum layers. Different lateral cell sizes and geometries allowed for setting up a broad range of oxygen superstructures  $\sigma$  at various coverages. The reciprocal space was sampled with  $\Gamma$ -centered grids adapted to these different cell sizes. For the  $2 \times 2$  cell, for instance, we used a  $17 \times 17$   $k$ -point mesh, which yields convergence to within 5 meV for adsorption energies and 0.5 meV for phase formation energies as compared to a  $19 \times 19$  mesh. For the other cells, the number of  $k$  points in each direction was scaled accordingly. Concerning the cutoff energy test calculations of the  $2 \times 2$  cell with 600 eV yielded changes of up to 2 meV in adsorption energies and below 0.1 meV for phase formation energies. The oxygen degrees of freedom as well as four Ir surface layers on each side were allowed to relax until the forces on the atoms were smaller than 0.01 eV/Å. Adsorption energies were referenced to the free O<sub>2</sub> molecule or alternatively the free O atom, which were both calculated in a cubic cell with 20 Å side length in a spin-polarized calculation using only the  $\Gamma$  point. To determine the zero-point energy (ZPE) of oxygen adsorbates, vibrational frequencies were calculated via a finite displacement scheme and diagonalization of the dynamical matrix as implemented in VASP. For these calculations, five-layer slabs with oxygen adsorbed on only one surface turned out to be sufficiently accurate. Due to their considerably higher mass, the Ir atoms were kept fixed at their (relaxed) positions during these calculations.

### III. THEORETICAL PREDICTION OF ORDERED PHASES

Oxygen binding energies were calculated according to

$$E_{\text{ads}}^{\text{mol}}(\sigma) = \frac{1}{N_{\text{O}}} \left( E(\sigma) - E_{\text{clean}} - N_{\text{O}} \frac{1}{2} E_{\text{O}_2} \right) \quad (1)$$

with respect to molecular oxygen, where  $E(\sigma)$  is the total energy of the given structure  $\sigma$ , and  $E_{\text{clean}}$  is the respective energy of the uncovered surface as evaluated in the same supercell. To facilitate a comparison to results from Johnson *et al.* [11] and Erikat *et al.* [14], we also determined  $E_{\text{ads}}^{\text{atom}}(\sigma)$  analogously to Eq. (1) using the energy of atomic oxygen  $E_{\text{O}}$  instead of that of molecular oxygen  $1/2 E_{\text{O}_2}$ . In Table I, we

TABLE I. Oxygen adsorption energies  $E_{\text{ads}}$  given in eV with respect to molecular (m) or atomic (a) oxygen for selected structures in comparison to published DFT values.

Structure	Coverage		This work	Ref. [11]	Ref. [14]	Ref. [15]
$(2 \times 2)$ -br	0.25	(a)	−5.261	−4.776	−5.22	
		(m)	−1.905			−2.03
$(2 \times 2)$ -h	0.25	(a)	−4.979	−4.526	−4.92	
		(m)	−1.622			
$(2 \times 2)$ -t	0.25	(a)	−4.464	−3.776	−4.37	
$(3 \times 1)$ -br(h)	0.33	(m)	−2.012			
$(3 \times 1)$ -br(a)	0.33	(m)	−1.587			−1.69
$(2 \times 1)$ -br(h)	0.50	(a)	−5.350	−4.908	−5.30	
		(m)	−1.994			−2.11
$(2 \times 1)$ -br(a)	0.50	(a)	−4.888	−4.459		
		(m)	−1.531			
$(1 \times 1)$ -br	1.00	(a)	−4.911		−4.87	
		(m)	−1.554			−1.70

compare our own values to those available in the literature. Structures are referred to by their Wood notation with the additional abbreviations “t” indicating top, “h” hollow, and “br” bridge sites. For O atoms being only one lattice vector apart from each other, two different local arrangements are possible. In the first one, neighboring O atoms do not share an Ir atom and line up along a hollow site. We therefore use a suffix “br(h)” for these structures. In the second configuration, adjacent O atoms share the Ir atom that lies in between them, so that those structures will be termed “br(a).” We note that in Ref. [11] such sites were referenced as “Bridge 1” and “Bridge 2,” respectively. In general, we find good agreement with the available literature values for  $E_{\text{ads}}$  with deviations for the bridge-site structures of 0.04–0.05 eV for Ref. [14], 0.10–0.15 eV for Ref. [15], and 0.43–0.49 eV for Ref. [11]. The main contribution to these differences arises most probably from the use of either a different exchange-correlation functional and/or ultrasoft pseudopotentials instead of the PAW method.

Moreover, we have determined the vibrational correction to the adsorption energy resulting from the change in vibrational frequencies—and thus the ZPE—upon adsorption. This correction term  $\Delta E_{\text{ads}}^{\text{vib}}$  was calculated for each structure  $\sigma$  according to

$$\Delta E_{\text{ads}}^{\text{vib}}(\sigma) = \frac{1}{2} \left( \sum_{i=1}^{3N_{\text{O}}} \hbar \omega_i - \frac{1}{2} \hbar \omega_{\text{O}_2} \right), \quad (2)$$

where  $\omega_i$  are the vibrational frequencies of adsorbed oxygen, and  $\omega_{\text{O}_2}$  is the stretching frequency of the free O<sub>2</sub> molecule. The latter was calculated to be 1565 cm<sup>−1</sup>, in good agreement with the experimental value of 1580 cm<sup>−1</sup> (cf. Ref. [32]). Throughout the following, we use these presumably more accurate ZPE-corrected values for the adsorption energies. A tabular comparison of uncorrected and corrected values is given in the supplemental material [33]. For structures with only bridge sites,  $\Delta E_{\text{ads}}^{\text{vib}}$  ranges from 0.02 to 0.03 eV per O atom, while for hollow sites it is around −0.02 eV, leading to a small relative energy gain of 0.04–0.05 eV for hollow sites. However, since the “single” hollow site (0.25 ML coverage)

is more than 0.25 eV less favorable than the bridge site, this represents only a small contribution and leaves the hierarchy of adsorption sites unchanged.

While the adsorption energy in Eq. (1) yields the correct hierarchy of adsorption structures at a *fixed coverage*, it does not allow for judging about the phase stability. To predict whether a specific adsorption phase is stable with respect to phase separation into the bare surface and the fully covered surface, we determine in direct analogy to the heat of formation for binary compounds (see, e.g., Refs. [34–36]) the *phase-formation energy* (cf. Refs. [37,38])

$$E_{\text{phase}}^0(\sigma) = \frac{1}{N_{\text{cell}}} [E(\sigma) - \theta E_{\text{full}}^{(1 \times 1)\text{-br}} - (1 - \theta) E_{\text{clean}}], \quad (3)$$

whereby the reference energies  $E_{\text{full}}^{(1 \times 1)\text{-br}}$  and  $E_{\text{clean}}$  are calculated in the same cell as the respective structure  $\sigma$  in order to avoid numerical inaccuracies arising from the use of different lateral cell sizes and shapes. Dividing by the number of lateral substrate unit cells  $N_{\text{cell}}$  makes  $E_{\text{phase}}^0$  the energetic difference per  $1 \times 1$  surface area of a certain structure  $\sigma$  to a phase-separated configuration weighted according to the respective coverage  $\theta$ . Again, we add a correction term  $\Delta E_{\text{phase}}^{\text{vib}}(\sigma)$  due to the zero-point energy,

$$E_{\text{phase}}(\sigma) = E_{\text{phase}}^0(\sigma) + \Delta E_{\text{phase}}^{\text{vib}}(\sigma), \quad (4)$$

which now reflects the difference between vibrational frequencies of oxygen arranged in the superstructure  $\sigma$  as compared to that in  $(1 \times 1)\text{-br}$ . A negative  $E_{\text{phase}}$  value indicates that the ordered structure  $\sigma$  is preferred over the phase separation into both  $1 \times 1$  phases. Accordingly, it has to be emphasized that only such a phase can be called a ground state of the system, which has a lower formation energy than any mixture of two other phases with the same (average) coverage. Note: In an  $E_{\text{phase}}$  versus  $\theta$  diagram, the formation energy of a phase mixture just corresponds to a straight line between the two limiting phases.

In the previous theoretical studies of O/Ir(100) $1 \times 1$ , only a small number of different adsorption geometries has been taken into account. Hence, a proper ground-state analysis could hardly be performed so far. In the present work, we now cover as much as 82 adsorption structures in total containing bridge as well as hollow sites in the coverage range between 0 and 0.5 ML. Since the top site is distinctly less favorable than the bridge site (0.8 eV at 0.25 ML, cf. Table I), the existence of energetically favorable structures with (partial) top site adsorption at any coverage is highly unlikely so that such structures were not considered. A total of 64 of the calculated structures have cell sizes up to  $N_{\text{cell}} = 8$ , while another 18 structures with even larger cells going up to  $N_{\text{cell}} = 18$  have been set up to accommodate  $3 \times 1$  and  $2 \times 1$  defect structures at low coverage. The choice of structures was partly governed by intuition and partly the result of a cluster expansion [39] using the mentioned DFT calculations as input. The phase formation and adsorption energies of a selection of energetically favorable structures are shown in Table II, and their relaxed geometries are shown in Fig. 2. A complete list of all structures that have been calculated by DFT in the framework of this study, including their energies

TABLE II. Adsorption and phase-formation energies of selected energetically favorable structures (bold: ground states). The adsorption site is br(h) for all structures and thus not explicitly displayed. The distance to the ground-state line  $\Delta E$  is also listed.

$\theta$ ML	$E_{\text{ads}}^{\text{mol}}(\sigma) _{\text{ZPE}}$ eV per O	$E_{\text{phase}}(\sigma)$ meV per $1 \times 1$	$\Delta E(\sigma)$	Structure $\sigma$
<b>0.50</b>	<b>-1.967</b>	<b>-223.2</b>	<b>0.0</b>	<b>2 × 1</b>
0.50	-1.942	-210.3	12.9	$c(2 \times 6)\text{-}3\text{O}$
0.50	-1.933	-206.2	17.0	$c(2 \times 4)\text{-}2\text{O}$
0.50	-1.920	-199.5	23.7	$(2 \times 3)\text{-}3\text{O}$
0.43	-1.969	-192.2	1.8	$(7 \times 1)\text{-}3\text{O}$
0.40	-1.971	-180.1	2.1	$(5 \times 1)\text{-}2\text{O}$
0.38	-1.977	-171.1	0.9	$(8 \times 1)\text{-}3\text{O}$
<b>0.33</b>	<b>-1.985</b>	<b>-154.8</b>	<b>0.0</b>	<b>3 × 1</b>
0.33	-1.976	-151.8	3.0	$(3 \times 6)\text{-}6\text{O}$
0.33	-1.974	-151.2	3.7	$(2 \times 6)\text{-}4\text{O}$
0.33	-1.967	-148.8	6.0	$(6 \times 1)\text{-}2\text{O}$
0.30	-1.977	-136.8	3.7	$(2 \times 5)\text{-}3\text{O}$
0.29	-1.974	-129.5	4.9	$(7 \times 1)\text{-}2\text{O}$
0.27	-1.984	-123.7	2.5	$(3 \times 5)\text{-}4\text{O}$
0.22	-2.001	-106.8	0.3	$(3 \times 6)\text{-}4\text{O}$
<b>0.20</b>	<b>-2.008</b>	<b>-97.6</b>	<b>0.0</b>	<b>(3 × 5)-3O</b>
<b>0.17</b>	<b>-2.017</b>	<b>-82.7</b>	<b>0.0</b>	<b>(3 × 4)-2O</b>
0.17	-2.007	-81.0	1.7	$(3 \times 6)\text{-}3\text{O}$
0.13	-2.014	-65.9	0.2	$(3 \times 5)\text{-}2\text{O}$
0.11	-2.009	-54.3	0.8	$(3 \times 6)\text{-}2\text{O}$

and real-space representations, is shown in the supplemental material [33].

The DFT phase-formation energies of all 82 structures are plotted as a function of their oxygen coverage in the surface stability diagram in Fig. 1. It is immediately apparent that for coverages below 0.5 ML, hollow site adsorption (dark blue circles) as well as a combination of bridge and hollow sites (light blue triangles) are energetically unfavorable, while in the most favorable structures oxygen adsorbs on bridge sites (red crosses). The ground-state line (GSL, shown in green) corresponds to the convex hull of the data points and indicates the energetically preferred phases as a function of the oxygen coverage. A total of four ground states (marked by green squares) are found by our calculations. The ones for lower coverages turn out to be only slightly superior to a phase mixture of  $2 \times 1$  and a clean  $1 \times 1$  surface marked by the black dashed line [which continues toward a still hypothetical  $(1 \times 1)\text{-br}$  phase]. Moreover, there are quite a few structures that are energetically not far off the ground-state line (cf. column 4 in Table II).

Starting at the known  $2 \times 1$  ground state at 0.5 ML, a second and as yet unreported ground state is found at 0.33 ML coverage: a  $3 \times 1$  structure with a br(h) configuration. It has a comparatively large binding energy of  $-2.01$  eV, which is slightly above the value for the  $2 \times 1$ . This is in apparent contrast to the results of Ma *et al.* [15], who find a particularly weak binding of only  $-1.69$  eV at 0.33 ML. Although they state in their paper that the energies of the “most favorable configurations” are given, Fig. 1 of Ref. [15] suggests that this energy actually corresponds to the  $(3 \times 1)\text{-br(a)}$  structure. For this we also find a similarly low adsorption energy of  $-1.59$  eV, which is 0.42 eV less favorable than the

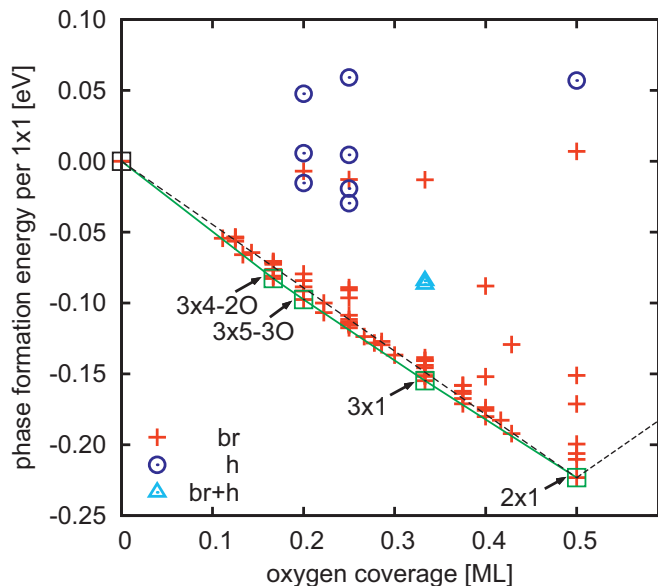


FIG. 1. Surface stability diagram up to the maximum coverage of 0.5 ML, which is experimentally accessible by  $O_2$  dosing. The ground-state line is shown in green and features two fundamental ground states, namely the  $3 \times 1$  and  $2 \times 1$  phases, with bridge-site occupation, as well as defect structures of the  $3 \times 1$  phase. The black dashed line corresponds to the energy of a phase mixture of  $2 \times 1$  and the clean unreconstructed surface or a (hypothetical)  $(1 \times 1)$ -br phase, respectively.

$(3 \times 1)$ -br(h) structure. Almost the same energetic difference (0.46 eV) exists between the  $(2 \times 1)$ -br(h) and  $(2 \times 1)$ -br(a) structures. Since the authors of Ref. [15] did not distinguish between the br(h) and br(a) sites [40] and apparently chose the less favorable  $3 \times 1$  structure, the new ground state identified here remained undetected in their study.

Between 0.33 and 0.5 ML oxygen coverage, all structures are located above the GSL (cf. Table II), indicating that phase separation into the  $2 \times 1$  and  $3 \times 1$  ground states is predicted. Structures that are closest to the GSL in this transition regime are of  $(n \times 1)$ -mO-br(h) type and represent ordered arrangements of  $3 \times 1$  and  $2 \times 1$  (see Fig. 2), which alternate in the direction perpendicular to the oxygen rows. Their distance to the GSL decreases with decreasing oxygen coverage, and the  $(8 \times 1)$ -3O structure at 0.38 ML is energetically almost degenerate with the phase separation. While at 0.5 ML there is a rather large energetic gap between the  $2 \times 1$  ground state and the excited states [ $c(2 \times 6)$ -3O,  $c(2 \times 4)$ -2O, and  $(2 \times 3)$ -3O shown in the top row of Fig. 2], this difference is also smaller for the  $3 \times 1$  ground state at 0.33 ML [ $(3 \times 6)$ -6O, Fig. 2, third row].

In the coverage regime below 0.33 ML, the preference for  $3 \times 1$  order continues. Several defect structures of  $3 \times 1$  are found at or very close to the GSL. They consist of regularly alternating stripes of  $3 \times 1$  and a clean surface. In the most favorable arrangements (Fig. 2, bottom row), the stripes of  $3 \times 1$  and the clean surface are both at least two atoms wide, so that a tiny energy gain can arise from a concerted local widening of the  $3 \times 1$  stripes (in order to increase the oxygen nearest-neighbor distance by about 0.1 Å) and a corresponding contraction of uncovered Ir rows (indicated by yellow arrows

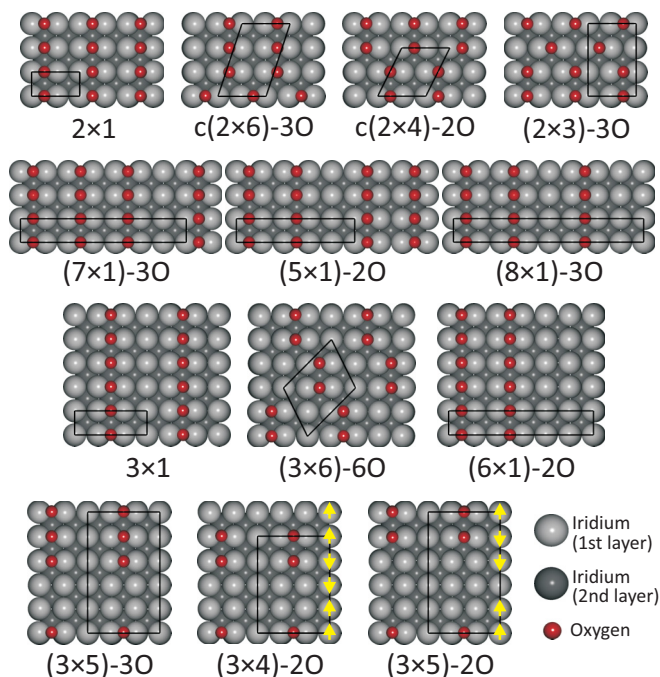


FIG. 2. Top view of energetically favorable structures selected from Table II. The adsorption site is br(h) for all displayed structures. Only the primitive unit cells are plotted in the ball models. Top row:  $\theta = 0.5$  ML. Second row:  $0.5 > \theta > 0.33$  ML. Third row:  $\theta = 0.33$  ML. Last row:  $\theta < 0.33$  ML. Arrows indicate lateral shifts of Ir rows.

in Fig. 2). Of course this lateral relaxation mechanism can only operate within quite narrow  $(3 \times 1)$ -ordered stripes and thus would in general favor the growth of narrow  $(3 \times 1)$ -ordered stripes over compact  $3 \times 1$  islands. For the  $(3 \times 4)$ -2O and  $(3 \times 5)$ -3O structures, the mutual distance between the two uncovered Ir rows decreases by 0.1 Å, while within the  $3 \times 1$  domains the Ir-Ir distance increases by about the same amount, so that at the domain boundary the Ir-Ir distance remains at the regular interatomic spacing. We anticipate that similar  $(3 \times n)$ -mO ( $m \leq n - 2$ ) structures with a br(h) configuration and even larger values of  $n$  than considered so far will also be close to the GSL of Fig. 1. However, calculating ever larger structures of the same type will hardly yield additional insight. The fact that for low coverage only  $(3 \times 1)$ -like structures are found at the GSL indicates that there is a clear tendency for oxygen atoms to adsorb in threefold distance to each other.

We note that the distinction of whether a  $(3 \times 1)$ -type defect structure is located right on the ground-state line or not might be based on sub-meV differences in  $E_{\text{phase}}(\sigma)$ , which is beyond the accuracy of the DFT calculations. Additionally, even for low temperatures those almost degenerate structures will coexist anyway. Therefore, it is expected that for coverages (sufficiently) below the ideal coverage of 0.33 ML, such  $3 \times 1$  stripes will develop in experiment as  $3 \times 1$  islands with strongly elongated shape, but without any *long-range* order, as is assumed in our model structures. Thus only two *fundamental* ground states are found for oxygen adsorption on the unreconstructed Ir(100) surface for coverages up to 0.5 ML:  $2 \times 1$  and  $3 \times 1$ . Selected model structures will be

discussed further in relation to the experimental observations in Secs. IV A and IV B.

#### IV. EXPERIMENTAL VERIFICATION AND STABILITY OF ORDERED PHASES

##### A. $2 \times 1$ phase at saturation coverage

The  $2 \times 1$  saturation phase of oxygen on the (unreconstructed) Ir(100) surface can either be prepared by dosing  $O_2$  at elevated temperatures just onto the stable and reconstructed  $5 \times 1$  phase [7,10], or—more commonly—onto the metastable  $1 \times 1$  phase, which has to be prepared before [6,11,12]. The latter procedure is the more remarkable one because the initial formation of the unreconstructed Ir(100)  $1 \times 1$  surface involves as a first step the cool-down in  $O_2$  atmosphere leading already to a  $2 \times 1$  LEED pattern at room temperature. So, the question remains whether anything is changed with oxygen reduction by  $H_2$  yielding the  $1 \times 1$  phase and subsequent oxygen readsorption. To find the best preparation recipe for a homogeneous  $2 \times 1$  phase, we have investigated different oxidation procedures by means of LEED and STM.

Dosing  $O_2$  at a rather low reaction temperature of 420 K on the reconstructed Ir(100)  $5 \times 1$  phase just lifts the surface reconstruction, but it leads to an only poorly ordered LEED pattern with rather faint and streaky spots [cf. Fig. 3(a)] in accordance with early observations by Küppers and Michel [7]. Subsequent heating to 620 K produces a  $2 \times 1$  LEED pattern with fairly sharp and intense superstructure spots and only weak remaining streaks along the  $\langle 011 \rangle$  directions [Fig. 3(b)]. Nevertheless, STM reveals numerous strongly elongated Ir islands on the surface as well as small Ir clusters or atoms [Fig. 3(c)]. The pronounced elongated form of the islands is a residue of the former  $5 \times 1$  domain orientation and can be explained by a zipperlike deconstruction process as described by Hammer *et al.* [41] for Fe/Ir(100) in combination with limited surface diffusion. Direct oxygen adsorption at 620 K on the reconstructed surface leads to practically the same LEED pattern as in Fig. 3(b) (therefore it is not shown here), but STM shows larger, more compact islands and fewer clusters [Fig. 3(d)]. This is due to the fact that single Ir atoms are now already sufficiently mobile when released in the deconstruction process, and thus they can immediately diffuse to an existing nucleus. When adsorbing at lower temperature, significant Ir diffusion starts only during the annealing step and thus the high initial adatom density also leads to a high density of nuclei.

To avoid the formation of Ir islands, much higher sample temperatures have to be applied. An upper limit for that is given by the temperature range in which oxygen gradually leaves the surface [800–1200 K; cf. Fig. 4(d)]. So, cooling down the surface under sufficiently high  $O_2$  flux should provide optimum conditions for both oxygen-induced restructuring and long-range Ir adatom diffusion. Indeed, this preparation yields an almost perfectly ordered  $2 \times 1$  phase with domain sizes extending over several hundreds of Å [Fig. 3(e)]. No Ir adatom islands are found anymore and only a few vacancy islands appear within the otherwise flat substrate terraces. Without atomic resolution, the oxygen rows are imaged in STM as straight and structureless lines [cf. Fig. 3(f)] with a mutual distance of twice the Ir lattice distance (5.43 Å).

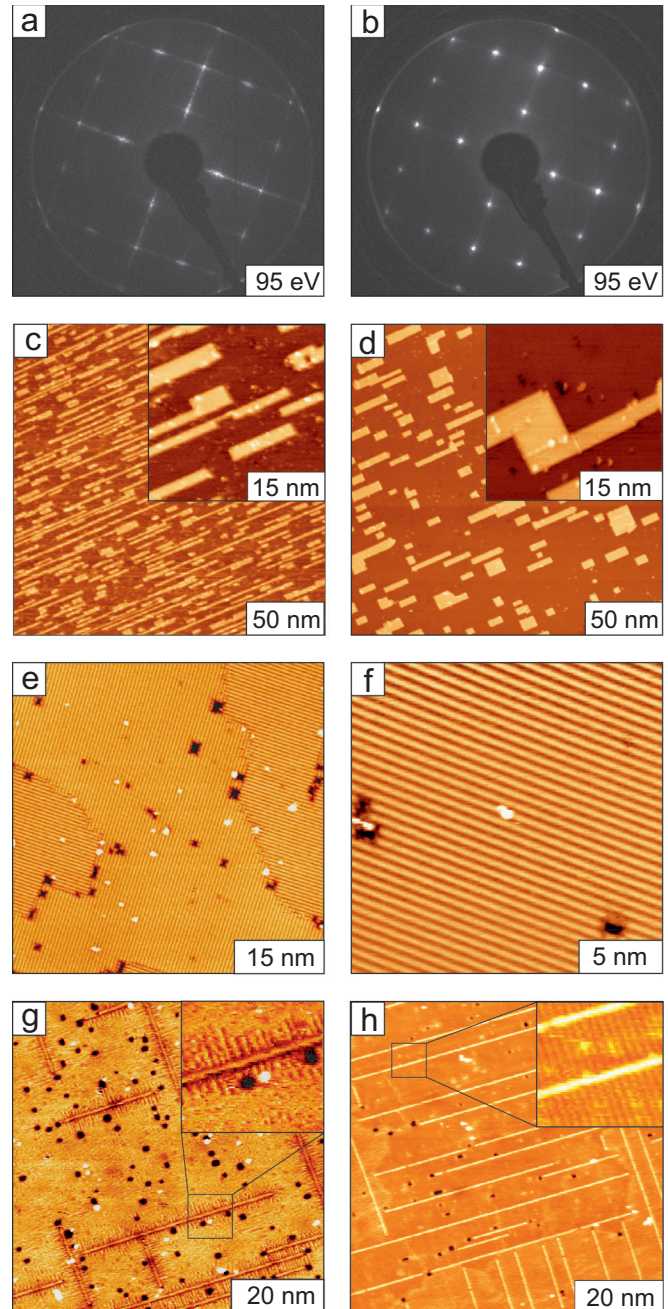


FIG. 3. Comparison of preparation procedures for the  $2 \times 1$  oxygen saturation phase. First row: (a) LEED patterns for the adsorption of 50 L  $O_2$  starting with a reconstructed Ir(100)  $5 \times 1$  surface at 420 K and (b) subsequently heated to 620 K. Second row: (c) STM images for the preparation under (b) and (d) oxygen being directly adsorbed at 620 K. Third row: (e) Wide area STM image and (f) closeup of the  $2 \times 1$  phase right after cool-down of the sample under continuous  $O_2$  flux. Bottom row: (g) Adsorption right on the unreconstructed Ir(100)  $1 \times 1$  surface at 300 K for a small coverage and (h) for a close-to-saturation coverage of oxygen.

Since the typical  $2 \times 1$  oxygen domains are significantly larger than the coherence width of our LEED optics ( $\leq 200$  Å), the corresponding diffraction spots become extremely sharp [cf. Fig. 4(a)].

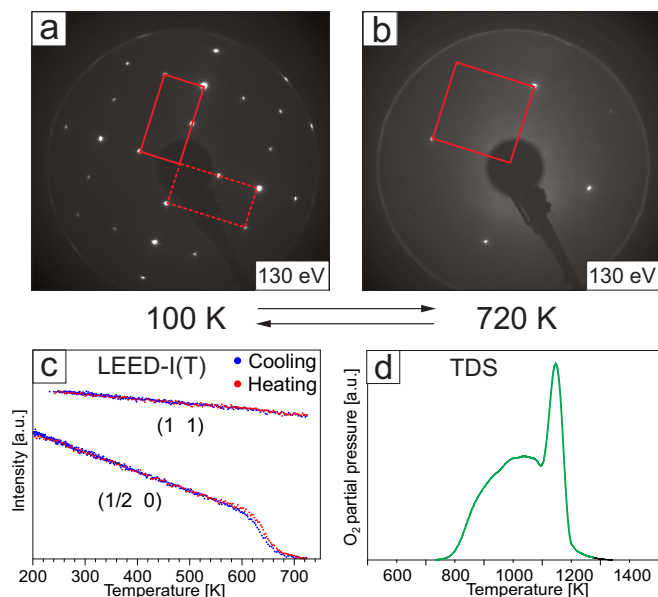


FIG. 4. LEED pattern of the Ir(100) surface with saturation coverage of oxygen taken at 100 K (a) and 720 K (b) showing  $2 \times 1$  and  $1 \times 1$  structures, respectively. Graph (c) displays the intensity variation of an integer and fractional order spot with temperature revealing a reversible phase transition. The  $O_2$ -thermodesorption spectrum (d) proves that no  $O_2$  desorbs during the temperature ramps performed in (c).

Surprisingly, when oxygen is adsorbed on the unreconstructed Ir(100)  $1 \times 1$  surface at room temperature or beyond, the development of single straight lines within the otherwise plain terraces is found already for very low exposures [Fig. 3(g)]. These lines protrude only a few tenths of an Å from the terraces (depending on the tunneling condition) and therefore they cannot be adatom islands as in the aforementioned case. Similar lines have been observed in earlier work at the nominally clean  $1 \times 1$  surface [5,42], and they were interpreted as “reconstruction lines,” i.e., single atomic rows of Ir shifted by half a surface lattice vector in the row direction. Here, the oxygen promoted reconstruction lines always start at or close to vacancy islands and serve as nucleation centers for ordered oxygen phases as indicated by their brushlike appearance. With further  $O_2$  exposure, the space between these reconstruction lines is increasingly filled up by oxygen forming the typical striplike pattern of the  $2 \times 1$  phase, when the coverage is close to maximum [Fig. 3(h)]. Eventually, for even higher  $O_2$  exposure also the reconstruction lines gradually disappear and the surface becomes completely covered by the  $2 \times 1$  phase, comparable to Fig. 3(e). We have indications that process parameters such as sample temperature and cleanliness severely influence the persistence of the lines. From that we infer that the best—and even the simplest—way to produce a well-ordered  $2 \times 1$  phase is the cool-down in  $O_2$  atmosphere as described above.

To investigate the thermal stability of the  $2 \times 1$  phase, we monitored the diffraction pattern during sample heating in UHV. At around 650 K we observe a phase transition toward  $1 \times 1$  order as demonstrated by the corresponding diffraction patterns displayed in Figs. 4(a) and 4(b) and the development of the spot intensities with temperature [Fig. 4(c)]. While the

integer order spots just show the regular intensity decrease due to the Debye-Waller factor, the fractional order spots vanish within the rather narrow temperature range of 620–680 K. The phase transition turns out to be fully reversible, since the intensities completely recover under subsequent cool-down with a small hysteresis of less than 10 K. The thermodesorption spectrum displayed in Fig. 4(d)—which is very similar to results published earlier [43]—proves that no oxygen leaves the surface during this transition, as long as the temperature is kept below  $\approx 740$  K.

The large difference of about 0.45 eV between the  $(2 \times 1)$ -br(h) and  $(1 \times 1)$ -br oxygen binding energies revealed by our DFT calculations (cf. Table I) indicates a significant effective O-O repulsion. Hence, the  $2 \times 1$  phase should be vastly stabilized against disorder, since any diffusion step of a single oxygen atom inevitably leads to a nearest-neighbor configuration as in the  $1 \times 1$  phase, when only bridge-site adsorption is assumed. The alternative switch toward a hollow site, which would lead to a somewhat larger O-O distance and hence to a reduced repulsion, seems also quite unlikely regarding the large energetic difference calculated already for single-site occupation (cf.  $2 \times 1$  phases in Table I). Another alternative to produce disorder within the  $2 \times 1$  structure is the formation of antiphase domains. We can estimate the formation energy of such domain boundaries perpendicular to the oxygen rows from the phase-formation energies of the structures  $c(2 \times 6)$ -3O,  $c(2 \times 4)$ -2O, and  $(2 \times 3)$ -3O displayed in the top row of Fig. 2. These structures can be regarded as  $2 \times 1$  phases with differently ordered domain-wall structures. From that we determine an energy cost of about 70 meV per oxygen row to form a single perpendicular domain boundary [ $N_{\text{cell}} \Delta E(\sigma)$  leads to 77, 68, or 71 meV for the three structures; cf. Table II], which appears likely to be the lowest energetic excitation of the system. Such a domain boundary would let adjacent domains scatter antiphase in the direction of fractional order spots and thus bring down their intensity very effectively. Hence, we propose that the observed phase transition is caused by a breakup of the homogeneous phase into smaller randomly distributed antiphase domains.

### B. Ordering at lower coverage— $3 \times 1$ phase

To investigate the whole coverage regime from the clean  $1 \times 1$  surface up to the saturation  $2 \times 1$  phase, we have continuously monitored the LEED pattern during  $O_2$  exposure for various temperatures. It turned out that perfect long-range ordering occurs already at temperatures as low as 120 K, at which oxygen must be very mobile on the surface. Only for even lower temperatures did we observe somewhat broader LEED spots as an indication for limited ordering due to kinetic hindrance. For temperatures below 200 K, we just found one more ordered structure—a  $3 \times 1$  phase at 0.33 ML coverage—as predicted by our DFT ground-state analysis. The development of this phase and its transition into the final  $2 \times 1$  phase is shown in Fig. 5 (left) by a series of LEED patterns taken for increasing  $O_2$  exposure at 120 K. On the right side of Fig. 5, the intensity along a line across the  $(0 1)$  and  $(1 1)$  spots (as indicated in the uppermost LEED pattern) is plotted as a function of  $O_2$  exposure. Superstructure spots start to develop right at third-order positions, which

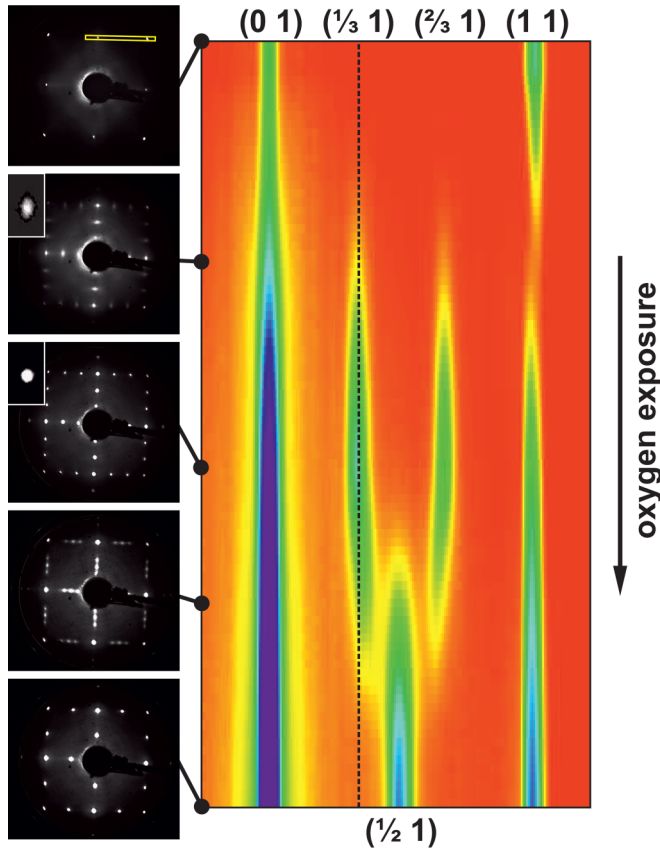


FIG. 5. Left: LEED patterns of the Ir(100) surface taken at 70 eV as a function of O<sub>2</sub> exposure at 120 K ranging from the clean surface (top) to saturation coverage (bottom). Insets display close-ups of the  $(-\frac{2}{3} 0)$  spot. Right: LEED intensity distribution taken along the line across the (0 1) and (1 1) beams shown in the topmost LEED pattern (logarithmic scale).

excludes any superstructure with a periodicity larger than threefold. From the onset of ordering, the superstructure spots are quite sharp in the profile direction, while perpendicular to that they are strongly elongated first and narrow only with increasing coverage (cf. the insets in the LEED patterns). We thus have a pronounced island growth of the  $3 \times 1$  phase whereby the islands grow preferentially in the direction of threefold periodicity. This can be taken as an indication that there is an attractive interaction between adjacent oxygen rows to align in threefold distance, which must be larger than any attraction along the rows. This observation is fully in line with the DFT prediction of a stripelike growth of  $3 \times 1$  domains derived from the structures of low-coverage ground states (cf. the last paragraph of Sec. III).

The formation of asymmetrically shaped islands can directly be observed in low-temperature STM, for which the sample was prepared at around 120 K and then cooled down to 77 K, i.e., we should see essentially a frozen equilibrium configuration. Figure 6(a) displays a survey scan for an oxygen coverage of 0.25 ML. Without resolving the single oxygen atoms within the rows, we just see homogeneous stripes with a predominantly threefold distance of 8.16 Å [see the inset of Fig. 6(a)]. The length of the stripes ranges from only 1 nm (4 atoms) to about 6 nm (22 atoms) at maximum, while in

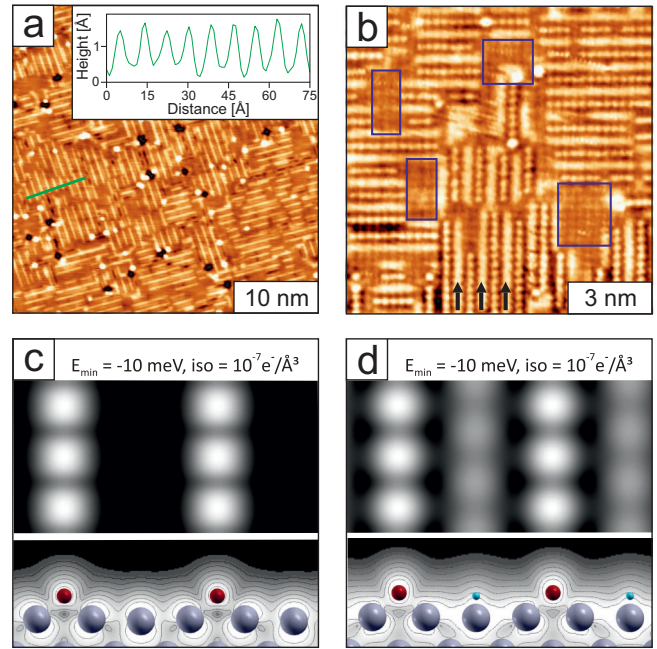


FIG. 6. (a) STM image taken at 77 K for an oxygen coverage of 0.25 ML coverage showing numerous  $(3 \times 1)$ -ordered islands. Inset: Height profile along the line indicated in the STM image. (b) STM image of the same preparation as in (a), but with atomic resolution taken at a bias voltage of  $U = -10$  meV ( $I = 1.0$  nA). The blue rectangles mark uncovered  $1 \times 1$  areas, while the black arrows indicate artificial lines, as discussed in the text. (c) Simulated STM image of the  $3 \times 1$  phase in top and side views. (d) Same as (c) but with an additional H atom at the central Ir row.

the perpendicular direction the islands typically extend over 10 nm or more. In a closeup image with true atomic resolution [Fig. 6(b)], we not only see the usually threefold distance of oxygen rows, but also the extended coexisting  $1 \times 1$  patches of a clean surface (the largest ones are marked by blue rectangles). This obvious phase separation is clear proof that there is indeed no other ground state for any oxygen coverage below 0.33 ML.

In the STM image displayed in Fig. 6(b), additional protruding lines are imaged in between the oxygen rows [some of them are marked by black arrows at the bottom of Fig. 6(b)], which do not correspond to O atoms. However, they can hardly be traced back to a mere electronic contrast, since our DFT simulation for the  $3 \times 1$  STM image does not show any hint of a protrusion of the central uncovered Ir row [Fig. 6(c)]. The artificial lines also appear—with somewhat reduced intensity—in the same 1.5-fold distance to the oxygen rows when there is no adjacent row present. Since the STM images were taken hours after preparation, we must expect some contamination due to postadsorption from the residual gas, in particular hydrogen, which is the dominant species there. To test the influence of coadsorbed hydrogen on the STM appearance of the  $3 \times 1$  phase, we performed another DFT simulation with one additional H atom in the unit cell [Fig. 6(d)]. As an adsorption site we have chosen the most reasonable bridge position at the central Ir row, which is not involved in the oxygen binding. From the striking similarity of the DFT simulation to the experimental STM appearance,

we conclude that the observed extra lines are just artefacts of the delayed STM data acquisition.

Turning back to Fig. 5, we see that after the completion of the  $3 \times 1$  phase, the superstructure spots start to shift toward the half-order position with further  $O_2$  exposure (cf. Fig. 5). This points toward a reduction of the average row spacing by introducing heavy domain walls, i.e., oxygen rows with only twofold mutual distance. However, this process does not continue until the  $(3 \times 1) \rightarrow (2 \times 1)$  transition is completed, as observed in other systems such as, e.g.,  $O/Ni(110)$  [44] or  $H/Ni(110)$  [45]. In contrast, here—as, e.g., in  $H/Rh(110)$  [46]—the intensity of the corresponding third-order spots quickly diminishes while a new superstructure spot at half-order position evolves. This means that we have a phase separation of  $3 \times 1$  and  $2 \times 1$  phases (the former slightly compressed) within almost the whole transition regime. This observation is again in perfect agreement with the predictions of the DFT ground-state analysis, where the model structures  $(8 \times 1)$ -3O,  $(5 \times 1)$ -2O, and  $(7 \times 1)$ -3O (cf. the second row of Fig. 2) can be regarded as ordered domain-wall structures in the transition regime between  $3 \times 1$  and  $2 \times 1$ . While the  $(8 \times 1)$ -3O ( $\Theta = 0.38$  ML) is still quasidegenerate ( $-2$  meV/oxygen) with a phase separation into  $3 \times 1$  and  $2 \times 1$ , the domain-wall structures become rapidly unfavorable with increasing coverage ( $\Theta = 0.40$  ML:  $-5$  meV/oxygen;  $\Theta = 0.43$  ML:  $-4$  meV/oxygen).

The  $(3 \times 1)$ -ordering turns out to be very sensitive to defects at the surface. It becomes, e.g., easily destroyed by a small amount of surface contaminations such as CO or atomic carbon. Also its thermal stability is rather low. Even a well-prepared  $3 \times 1$  phase undergoes an order-disorder transition already at temperatures below 200 K as displayed in Fig. 7(a). In contrast to the  $2 \times 1$  phase, the phase transition here is not fully reversible. If, for example, the temperature is raised further, the third-order spots surprisingly start to reappear at 230 K and the thermally induced order-disorder transition is shifted to a higher temperature of about 300 K. Upon cool-down, the intensity of the third-order spots recovers to some extent, but it does not reach the former level anymore. The reason for this peculiar behavior is the irreversible formation of reconstruction lines (as described in the previous subsection) upon annealing. These lines stabilize the  $3 \times 1$  phase in their vicinity, so that

even at room temperature  $3 \times 1$  islands can renucleate there. By this “trick” the  $3 \times 1$  phase can also be imaged at room temperature by STM, as demonstrated in Fig. 7(b).

The rather low order-disorder transition temperature of the  $3 \times 1$  phase can be estimated from our DFT calculations as well. Other than in the  $2 \times 1$  phase, an oxygen atom moving one step out of its row does not feel a strong repulsion from the opposing row. The energetic penalty of such a single-atom process cannot directly be derived from our calculations, but as a lower limit we can estimate the energy cost for a concerted sideways shift of a complete oxygen row. This leads to a combined light and heavy domain wall, which is just modeled by the  $(6 \times 1)$ -2O structure (Fig. 2, third row). From that we calculate an energetic expense as small as 36 meV per moved oxygen atom [ $N_{\text{cell}} \Delta E(\sigma)$ , cf. Table II]. However, as in the case of the  $2 \times 1$  phase, the smallest energy cost is associated with a domain boundary formation perpendicular to the oxygen row direction. From the structure  $(3 \times 6)$ -6O (Fig. 2, third row), which is a phase with perpendicular domain boundaries after every two oxygen atoms, we estimate this boundary formation energy to be as low as 18 meV per oxygen row, about four times smaller than in the case of the  $2 \times 1$  phase. This scales nicely with the ratio of disordering temperatures of the two phases, which further supports the idea that perpendicular domain boundary creation might be the relevant step in the disordering process. It also proves that the single oxygen row is not at all a very stable structural element of the system, as one might anticipate from the occurrence of  $n \times 1$  structures only.

## V. CRYSTALLOGRAPHIC STRUCTURE OF THE ORDERED PHASES

After having investigated the appearance and stability of the two ordered phases  $Ir(100) 3 \times 1$  and  $Ir(100) 2 \times 1$ , we now determine their crystallographic structures as precisely as possible in order to compare the experimental results with the predictions of the fully relaxed DFT structures. For that we have recorded huge LEED intensity data sets for both phases with accumulated total energy widths in the order of 10 000 eV each. The database for the  $3 \times 1$  phase comprises 31 inequivalent beams (9 integer, 22 fractional order), and that of the  $2 \times 1$  phase comprises 27 beams (11 integer, 16 fractional order). These large databases allowed us to vary up to 21 and 17 parameters for the  $3 \times 1$  and  $2 \times 1$  phases, respectively. Even then redundancy factors  $\rho > 20$  resulted, i.e., we still had more than 20 times as much data as needed for the analyses. In the LEED calculations, we only considered the br(h) site (cf. Fig. 8, top row), because of its large advantage in binding energy compared to all other sites (cf. Table I). This choice was confirmed by excellent agreement between experimental and best-fit spectra expressed by extremely low reliability factors  $R_p = 0.119$  ( $3 \times 1$ ) and 0.090 ( $2 \times 1$ ). Due to the low  $R_p$ -factor level and the large databases, the variances of the  $R_p$ -factors also become extremely low, and hence exceptionally small error margins for the fitted parameters result—partly below 1 pm.

To give an impression about the quality of the LEED fits, some experimental and calculated best-fit spectra are displayed in Fig. 9, selected in a way that single-beam  $R_p$ -factors are close to the total  $R_p$ -factors of the analyses. The complete

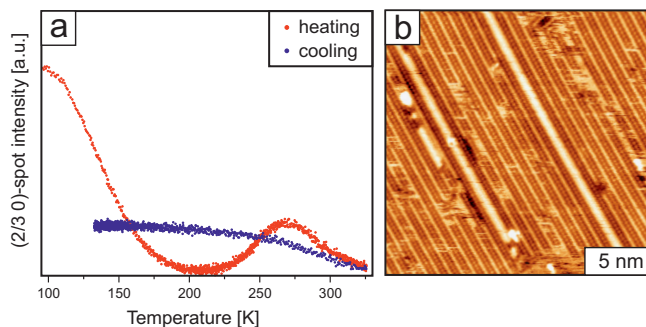


FIG. 7. (a) Intensity variation of the  $(2/3 0)$  spot of the  $3 \times 1$  phase with temperature revealing a partly irreversible transformation of the surface via formation of reconstruction lines. (b) Room-temperature STM image of a  $(3 \times 1)$ -ordered area stabilized by reconstruction lines (imaged as broad bright lines).

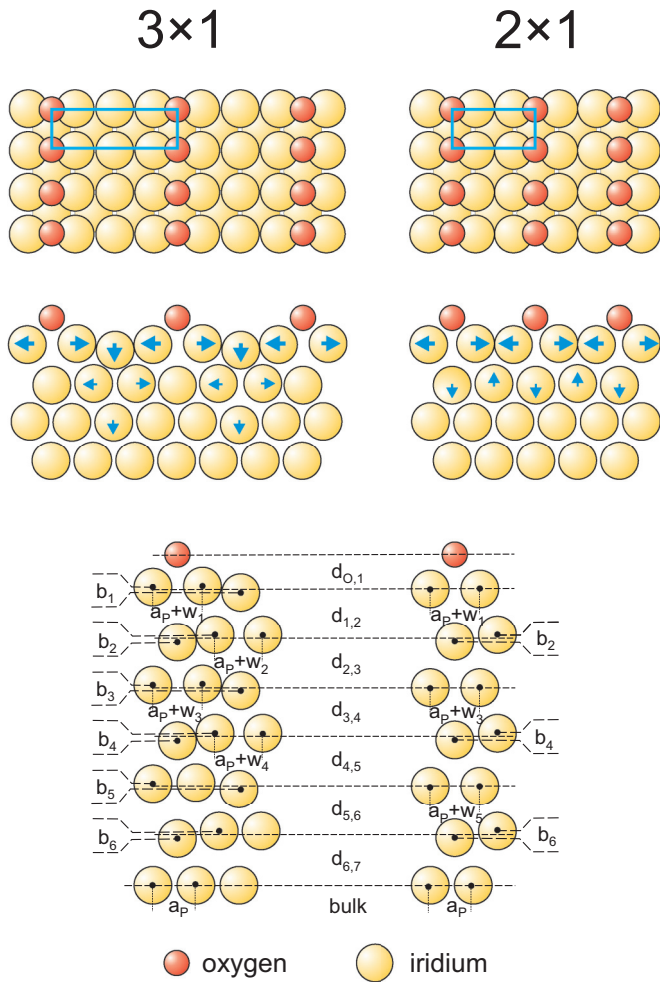


FIG. 8. Upper part: Ball models of the  $3 \times 1$  and  $2 \times 1$  structures in top and side views. Blue arrows indicate relevant atomic movements. Lower part: Definition of structural parameters compiled in Table III. The relative atomic arrangements are displayed for positive parameter values.

sets of spectra can be found both as data files and in graphical representation in the supplemental material [33]. A compilation of all fitted quantities is given in Table III together with the respective errors derived from “error curves” ( $R_p$  versus parameter variation), which are also collected in the supplemental material [33]. As usual for LEED analyses, the atomic coordinates are translated into average distances of surface-parallel layers as well as intralayer atomic relaxations such as vertical bucklings or variations of lateral spacings. A definition of all used quantities is given in the lower part of Fig. 8. For comparison, Table III also contains the result of the former LEED analysis by Johnson *et al.* [11] for the  $2 \times 1$  phase as well as the corresponding values from the fully relaxed DFT structures. Unfortunately, no detailed structural parameters are available from former DFT studies [11,14,15].

In both analyzed phases, very similar oxygen-iridium bond lengths are found with 1.93 Å ( $3 \times 1$ ) and 1.92 Å ( $2 \times 1$ ), resulting in quite typical covalent radii of oxygen of 0.57 and 0.56 Å, respectively. The fits further reveal substantial geometrical relaxations of substrate atoms underneath the adsorbates, which extend with statistically significant amplitudes down to

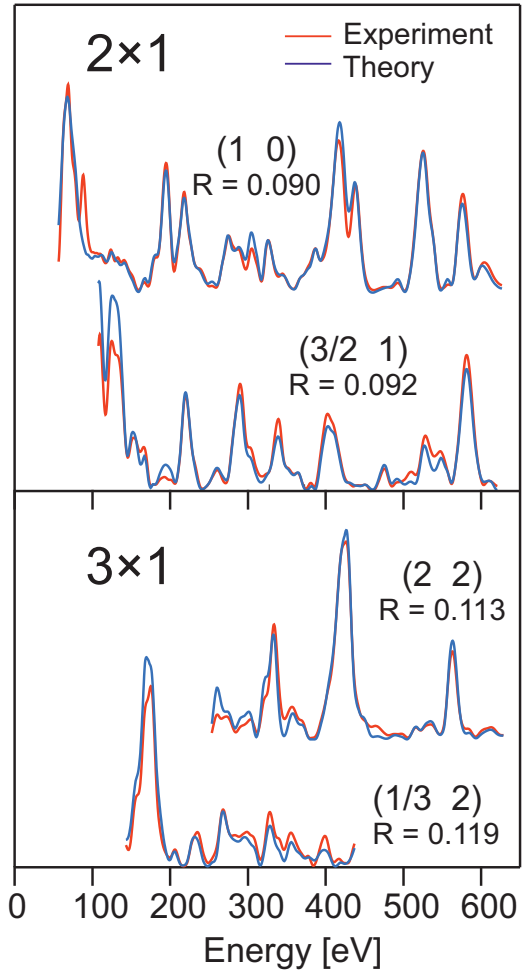


FIG. 9. Selected experimental and best-fit spectra for the  $3 \times 1$  and  $2 \times 1$  phases demonstrating the quality of the fits. The full data sets are reproduced in the supplemental material [33].

the third layer as visualized by the arrows in Fig. 8, center row. Physically reasonable substrate relaxations—though not outside the error bars of the  $I(E)$  analyses—can even be found in deeper layers; cf. Table III. It appears quite obvious that this relaxation pattern is the elastic response of the substrate toward the tendency of the O adatoms to penetrate deeper into the surface thereby pushing the Ir binding partners apart. This lateral widening of the Ir-Ir distance is rather substantial and somewhat larger for the  $3 \times 1$  phase (0.18 Å) than for the  $2 \times 1$  phase (0.15 Å), since the local bond widening has to be compensated within either three or only two Ir bond distances for the two phases, respectively. The third Ir surface atom in the  $3 \times 1$  unit cell, which is not in contact with oxygen, is lowered by the buckling amplitude  $b_1$  resulting in a vertical distance to the underlying Ir atoms of 1.82 Å. In principle, this effect could be caused by elastic strain in the surface. However, this distance is very close to the corresponding value of 1.85 Å for the clean Ir(100) surface [5]. Therefore, it is more likely to regard the Ir atoms bound to oxygen as lifted upward instead, which is a typical behavior in chemisorption systems.

For the  $2 \times 1$  phase, our LEED analysis yields virtually the same crystallographic structure as the former study by Johnson *et al.* [11] with numerical deviations smaller than 0.01 Å

TABLE III. Compilation of relevant parameters and error margins for the  $3 \times 1$  and  $2 \times 1$  phases. Structural parameters and vibrational amplitudes are given in Å; the former are specified in Fig. 8.  $u_{\text{O}}$ ,  $u_{\text{IrOb}}$ , and  $u_{\text{IrOf}}$  denote the rms vibrational amplitudes for oxygen, O-bound, and O-free top-layer Ir atoms.  $\Delta E$  and  $\rho$  are the cumulated energy range and the redundancy factor of the LEED analysis, and “var” denotes the variance of the Pendry  $R_P$ -factor.

	$3 \times 1$		$2 \times 1$		Ref. [11] LEED
	This work		This work		
	LEED	DFT	LEED	DFT	
Average layer distances					
$d_{0,1}$	1.286 <sup>+0.012</sup> <sub>-0.013</sub>	1.274	1.293 <sup>+0.006</sup> <sub>-0.006</sub>	1.266	1.301 <sup>+0.034</sup> <sub>-0.034</sub>
$d_{1,2}$	1.883 <sup>+0.006</sup> <sub>-0.006</sub>	1.870	1.902 <sup>+0.003</sup> <sub>-0.004</sub>	1.897	1.898 <sup>+0.027</sup> <sub>-0.027</sub>
$d_{2,3}$	1.930 <sup>+0.006</sup> <sub>-0.006</sub>	1.925	1.926 <sup>+0.004</sup> <sub>-0.004</sub>	1.921	1.914 <sup>+0.034</sup> <sub>-0.034</sub>
$d_{3,4}$	1.923 <sup>+0.007</sup> <sub>-0.007</sub>	1.921	1.921 <sup>+0.004</sup> <sub>-0.004</sub>	1.919	n. v.
$d_{4,5}$	1.920 <sup>+0.010</sup> <sub>-0.009</sub>	1.915	1.919 <sup>+0.005</sup> <sub>-0.005</sub>	1.915	n. v.
$d_{5,6}$	1.918 <sup>+0.012</sup> <sub>-0.012</sub>	n. v.	1.920 <sup>+0.006</sup> <sub>-0.006</sub>	n. v.	n. v.
$d_{6,7}$	1.931 <sup>+0.014</sup> <sub>-0.014</sub>	n. v.	1.925 <sup>+0.006</sup> <sub>-0.007</sub>	n. v.	n. v.
Vertical buckling amplitudes					
$b_1$	0.093 <sup>+0.012</sup> <sub>-0.013</sub>	0.112			
$b_2$	0.010 <sup>+0.012</sup> <sub>-0.014</sub>	0.022	0.038 <sup>+0.007</sup> <sub>-0.009</sub>	0.067	0.038 <sup>+0.034</sup> <sub>-0.034</sub>
$b_3$	0.025 <sup>+0.014</sup> <sub>-0.012</sub>	0.033			
$b_4$	0.003 <sup>+0.018</sup> <sub>-0.016</sub>	0.001	0.008 <sup>+0.009</sup> <sub>-0.009</sub>	0.009	n. v.
$b_5$	0.003 <sup>+0.020</sup> <sub>-0.020</sub>	n. v.			
$b_6$	0.005 <sup>+0.029</sup> <sub>-0.030</sub>	n. v.	0.005 <sup>+0.020</sup> <sub>-0.015</sub>	n. v.	n. v.
Lateral bond widening amplitudes					
$w_1$	0.180 <sup>+0.030</sup> <sub>-0.029</sub>	0.198	0.145 <sup>+0.022</sup> <sub>-0.023</sub>	0.151	0.150 <sup>+0.059</sup> <sub>-0.059</sub>
$w_2$	0.040 <sup>+0.027</sup> <sub>-0.027</sub>	0.046			
$w_3$	0.005 <sup>+0.022</sup> <sub>-0.023</sub>	0.011	-0.005 <sup>+0.014</sup> <sub>-0.018</sub>	-0.005	n. v.
$w_4$	0.005 <sup>+0.031</sup> <sub>-0.029</sub>	0.011			
$w_5$	n. v.	n. v.	-0.005 <sup>+0.026</sup> <sub>-0.024</sub>	n. v.	n. v.
Surface atom vibrational amplitudes					
$u_{\text{O}}$	0.120 <sup>+0.019</sup> <sub>-0.020</sub>		0.108 <sup>+0.012</sup> <sub>-0.013</sub>		0.153 (n. v.)
$u_{\text{IrOb}}$	0.058 <sup>+0.020</sup> <sub>-0.028</sub>		0.063 <sup>+0.014</sup> <sub>-0.014</sub>		0.051 (n. v.)
$u_{\text{IrOf}}$	0.050 <sup>+0.026</sup> <sub>-0.050</sub>				
LEED fit characteristics					
$\Delta E$	10 150 eV		9819 eV		2005 eV
$R_P$	0.119		0.090		0.179
var.	0.008		0.006		0.025
$\rho$	21.0		25.1		16.7

for all parameters varied in both analyses. However, we have quantified additionally a number of minor relaxations within deeper layers, and in particular the overall error margins could be drastically reduced. This high *precision* of the structure determination also holds for the as yet undetected  $3 \times 1$  phase. The results of our LEED analyses also coincide closely with the predictions of the corresponding DFT model calculations having rms deviations of parameter values as small as 0.01 Å for both phases. This means that two completely independent methods optimizing totally different quantities ( $R_P$ -factor versus slab energy) result in virtually the same parameter values (within the small error bars given by LEED). This

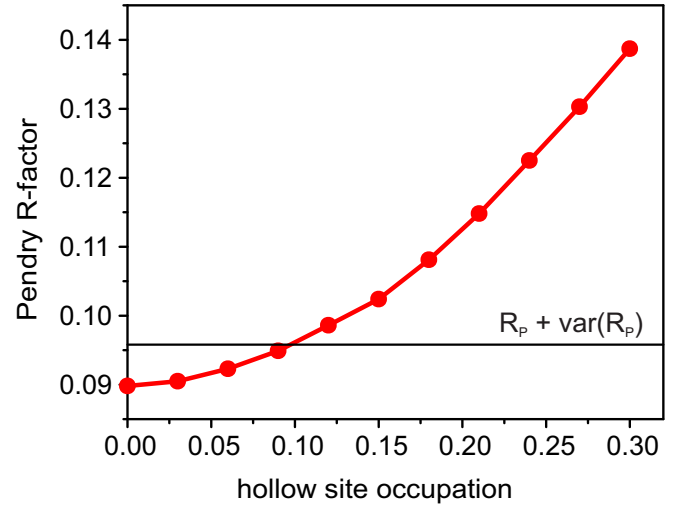


FIG. 10. Development of the Pendry  $R$ -factor as a function of hollow site occupation in between the  $2 \times 1$  oxygen rows by additional O atoms.

strongly indicates that systematic errors are quite negligible here, and therefore also the *accuracy* of our LEED analyses (as well as that of the DFT predictions) lies in the picometer range.

Finally, we also checked for the existence of additional O atoms randomly adsorbed in hollow sites between the oxygen rows of the  $2 \times 1$  phase as proposed by Sander *et al.* [12]. For various given occupation probabilities for the hollow sites (0–30% with 3% increments), we performed complete *all-parameter* structural searches in order to avoid any influence of possible parameter couplings. The resulting best-fit  $R_P$ -factors are plotted against the respective oxygen hollow site occupation in Fig. 10. Obviously, there is a clear minimum for zero coverage, i.e., hollow site oxygen can be excluded with an error of 10% ( $\Delta\Theta = 0.05$  ML) determined as usual via the variance level of the  $R_P$ -factor. This proves that at least for dosing  $\text{O}_2$  the maximum coverage for the Ir(100) surface does not exceed  $\Theta = 0.5$  ML.

## VI. CONCLUSION

In the present study, the structure and ordering of oxygen on the unreconstructed Ir(100) surface was investigated by a concerted application of both experimental (LEED, STM) and theoretical methods (DFT). The analysis was confined to the coverage regime  $\Theta \leq 0.5$  ML, which is the maximal range experimentally accessible when dosing molecular oxygen. On the theory side, we placed particular emphasis on the identification of the ground-state phases of the system and their structural and energetic properties, which were not addressed so far in previous studies. For that, a vast number of model structures were calculated and their formation energies compared, not only with each other but also with any possible mixture of phases. On this basis, we could clearly show that there are only two fundamental ground states of adsorbed oxygen in the whole investigated coverage regime, which are the known  $2 \times 1$  phase at  $\Theta = 0.5$  ML and an as yet undetected  $3 \times 1$  phase at  $\Theta = 0.33$  ML. In our experiments, we could verify exactly these two ordered phases and study their thermal stability and coverage-dependent transitions. The

observed pronounced phase-separation regimes between clean surfaces,  $3 \times 1$  and  $2 \times 1$ , were taken as a further argument that there are no other ground states in the system. Moreover, many experimentally observed details of the phase transitions with coverage and temperature could be deduced and understood from an analysis of the energetics of calculated model defect structures. In particular, it was shown that the single oxygen rows are not very stable structural elements of the system as formerly assumed, since their breakup by perpendicular domain boundaries is found to have the lowest (collective) excitation energy.

Both ordered oxygen structures were also crystallographically characterized by means of LEED intensity analyses yielding an excellent quality of fit to the extended databases collected experimentally. We could show that the local binding configuration of oxygen is practically the same for both phases, however the induced geometrical relaxations of substrate atoms vary due to the different periodicity of the phases. It is also noteworthy that all structural parameters derived in the course of the LEED analyses coincide with those predicted by DFT on the picometer scale.

Additionally, we could show in this study that the tendency of the Ir(100) surface to reconstruct affects the ordering behavior of oxygen much more than expected. Only by means of STM, could we show that local reconstruction lines already develop around room temperature at the surface except for the clean and the fully oxygen saturated case. It was demonstrated that these lines are able to stabilize at least the  $3 \times 1$  phase and act also as nucleation centers for this phase. A detailed investigation of the interrelation between these local reconstruction elements and the adsorbed oxygen, however, is beyond the scope of this paper.

Last but not least, we want to point out that the present study may serve as a prime example of a supposedly simple adsorption system such as O/Ir(100) that still exhibits a rather complex ordering behavior. This complexity, however, can be elucidated and understood in great detail by an intimate and smart combination of experimental observation and theoretical modeling. The study also demonstrates the extreme accuracy with which surface structures can nowadays be determined experimentally and how closely the predictions from *ab initio* methods can match the experimental values.

- 
- [1] D. G. Fedak and N. A. Gjostein, *Surf. Sci.* **8**, 77 (1967).
- [2] P. Heilmann, K. Heinz, and K. Müller, *Surf. Sci.* **83**, 487 (1979).
- [3] M. A. Van Hove, R. J. Koestner, P. C. Stair, J. P. Bibérian, L. L. Kesmodel, I. Bartos, and G. A. Somorjai, *Surf. Sci.* **103**, 189 (1981); **103**, 218 (1981).
- [4] E. Lang, K. Müller, K. Heinz, M. A. Van Hove, R. J. Koestner, and G. A. Somorjai, *Surf. Sci.* **127**, 347 (1983).
- [5] A. Schmidt, W. Meier, L. Hammer, and K. Heinz, *J. Phys.: Condens. Matter* **14**, 12353 (2002).
- [6] J. T. Grant, *Surf. Sci.* **18**, 228 (1969).
- [7] J. Küppers and H. Michel, *Appl. Surf. Sci.* **3**, 179 (1979).
- [8] L. Hammer, W. Meier, A. Klein, P. Landfried, A. Schmidt, and K. Heinz, *Phys. Rev. Lett.* **91**, 156101 (2003).
- [9] T. J. Lerotholi, G. Held, and D. A. King, *Surf. Sci.* **601**, 1285 (2007).
- [10] T. N. Rhodin and G. Brodén, *Surf. Sci.* **60**, 466 (1976).
- [11] K. Johnson, Q. Ge, S. Titmuss, and D. A. King, *J. Chem. Phys.* **112**, 10460 (2000).
- [12] D. Sander, H. L. Meyerheim, Z. Tian, L. Niebergall, N. N. Negulyaev, K. Mohseni, V. S. Stepanyuk, R. Felici, and J. Kirschner, *Phys. Rev. B* **81**, 153403 (2010).
- [13] L. Hammer, P. Ferstl, A. Michl, S. Müller, and M. A. Schneider (unpublished).
- [14] L. A. Erikat, B. A. Hamad, and J. M. Khalifeh, *Eur. Phys. J. B* **67**, 35 (2009).
- [15] S. H. Ma, Z. Y. Jiao, X. Z. Zhang, Z. X. Yang, and X. Q. Dai, *Eur. Phys. J. B* **85**, 216 (2012).
- [16] P. Feulner and D. Menzel, *J. Vac. Sci. Technol.* **17**, 662 (1980).
- [17] K. Heinz, G. Schmidt, L. Hammer, and K. Müller, *Phys. Rev. B* **32**, 6214 (1985).
- [18] K. Heinz, *Rep. Prog. Phys.* **58**, 637 (1995).
- [19] V. Blum and K. Heinz, *Comp. Phys. Commun.* **134**, 392 (2001).
- [20] J. Rundgren, *Phys. Rev. B* **68**, 125405 (2003).
- [21] J. W. Arblaster, *Platinum Met. Rev.* **54**, 93 (2010).
- [22] M. A. Van Hove and S. Y. Tong, *Surface Crystallography by LEED*, Springer Series in Chemistry and Physics Vol. 2 (Springer, Berlin, 1979).
- [23] J. B. Pendry, *J. Phys. C* **13**, 937 (1980).
- [24] G. Kresse and J. Hafner, *Phys. Rev. B* **47**, 558(R) (1993).
- [25] G. Kresse and J. Hafner, *Phys. Rev. B* **49**, 14251 (1994).
- [26] G. Kresse and J. Furthmüller, *Comput. Mater. Sci.* **6**, 15 (1996).
- [27] G. Kresse and J. Furthmüller, *Phys. Rev. B* **54**, 11169 (1996).
- [28] P. E. Blöchl, *Phys. Rev. B* **50**, 17953 (1994).
- [29] G. Kresse and D. Joubert, *Phys. Rev. B* **59**, 1758 (1999).
- [30] J. P. Perdew, K. Burke, and M. Ernzerhof, *Phys. Rev. Lett.* **77**, 3865 (1996).
- [31] M. Methfessel and A. T. Paxton, *Phys. Rev. B* **40**, 3616 (1989).
- [32] K. P. Huber and G. Herzberg, *Molecular Spectra and Molecular Structure. IV. Constants of Diatomic Molecules* (Van Nostrand Reinhold, New York, 1979).
- [33] See Supplemental Material at <http://link.aps.org/supplemental/10.1103/PhysRevB.93.235406> for a compilation of all calculated, fully relaxed DFT structures (table and ball models), and for data files and graphs comprising all experimental and best-fit LEED spectra together with the error determination for the LEED best-fit parameters.
- [34] A. Zunger, L. Wang, G. Hart, and M. Sanati, *Modell. Simul. Mater. Sci. Eng.* **10**, 685 (2002).
- [35] S. V. Barabash, V. Blum, S. Müller, and A. Zunger, *Phys. Rev. B* **74**, 035108 (2006).
- [36] S. B. Maisel, T. C. Kerscher, and S. Müller, *Acta Mater.* **60**, 1093 (2012).
- [37] H. Tang, A. Van der Ven, and B. L. Trout, *Phys. Rev. B* **70**, 045420 (2004).
- [38] D. Lerch, O. Wieckhorst, L. Hammer, K. Heinz, and S. Müller, *Phys. Rev. B* **78**, 121405(R) (2008).
- [39] J. M. Sanchez, F. Ducastelle, and D. Gratias, *Physica A* **128**, 334 (1984).
- [40] S. H. Ma (private communication).

- [41] L. Hammer, W. Meier, A. Schmidt, and K. Heinz, *Phys. Rev. B* **67**, 125422 (2003).
- [42] G. Gilarowski, J. Méndez, and H. Niehus, *Surf. Sci.* **448**, 290 (2000).
- [43] T. Ali, B. Klötzer, A. V. Walker, Q. Ge, and D. A. King, *J. Chem. Phys.* **109**, 9967 (1998).
- [44] L. H. Germer, J. W. May, and R. J. Szostak, *Surf. Sci.* **7**, 430 (1967).
- [45] V. Penka, K. Christmann, and G. Ertl, *Surf. Sci.* **136**, 307 (1984).
- [46] W. Nichtl-Pecher, J. Gossmann, W. Stammer, G. Besold, L. Hammer, K. Heinz, and K. Müller, *Surf. Sci.* **249**, 61 (1991).